Chem. Mater. **1997,** *9,* 270−277

Structural Evolution and Electronic Properties of $La_{1+x}Sr_{2-x}Mn_2O_7$

R. Seshadri, C. Martin, M. Hervieu, and B. Raveau*

Laboratoire CRISMAT, CNRS URA 1318, ISMRA et Université de Caen,
Bd. du Maréchal Juin, 14050 Caen Cedex, France

C. N. R. Rao

Solid State and Structural Chemistry Unit and CSIR Center of Excellence in Chemistry,
Indian Institute of Science, Bangalore 560 012, India

Received June 18, 1990. Revised Manuscript Received August 28, 1996[⊗]

A detailed study of the layered manganite $La_{1+x}Sr_{2-x}Mn_2O_7$ has been performed, establishing that within the composition range $0.1 \leq x \leq 0.45$ the phases crystallize in the $I4/mmm$ space group. The evolution of structural parameters with x in this composition range has been followed using a novel application of an existing program for the Rietveld analysis of powder diffraction data. The structure, a familiar intergrowth of rock-salt (La,Sr)O slabs and double perovskite $(La,Sr)_2Mn_2O_6$ units, is characterized by a reluctance to deform the latter. This manifests as a "pumping" of the larger Sr^{II} ion into the 12-coordinate site of the structure as x is increased. We report these features of the structure as well as electrical transport and magnetic properties, in light of recent observations of giant, negative magnetoresistance in these systems.

Introduction

The observation of giant, negative magnetoresistance (GMR) in rare-earth manganites with the perovskite structure[1,2] has given rise to a flurry of activity, with a number of recent studies involving the search for dramatic effects,[3−6] structure−property correlations,[7−9] and the associated phenomena of charge and magnetic ordering.[10−12] These perovskites are usually formulated $A^{III}_{1-x}A'^{II}_{x}MnO_3$, where A is a rare-earth ion and A′ an alkaline-earth ion, and there is now a considerable body of information pointing to the role of size and charge of the $A^{III}_{1-x}A'^{II}_{x}$ combination. It is of interest to examine related oxide systems that display GMR effects, from the viewpoint of both phenomena and application. The pyrochlore $Tl_2Mn_2O_7$[13,14] and the layered perovskite $La_{1.2}Sr_{1.8}Mn_2O_7$[15,16] have also been demonstrated as displaying GMR effects. Studies of the latter are particularly important to the understanding of structure and magnetotransport properties in the perovskite systems because of the similar environment around Mn in the structure which, for $(La, Sr)_3Mn_2O_7$[17] is that of the $m = 2$ member of the so called Ruddlesden−Popper phases $(SrO)(SrTiO_3)_m$.[18] These phases are intergrowths of rock-salt like SrO slabs with m-tuple slabs of the perovskite $SrTiO_3$. In the terminology of structurally related cuprate superconductors, this $m = 2$ member is referred to as the "0212" phase.[19] The structure of $(La,Sr)_3Mn_2O_7$ is shown in Figure 1. While there is a single site for the A cation in the perovskite $AMnO_3$, in the "0212" structure, there are two sites for the A cations (corresponding to R and P in Figure 1) allowing a greater degree of structural tuning in terms of size and charge. Apart from this, the "0212" structure is quasi-two-dimensional, involving modes of magnetic ordering that would be quite different from what is observed in the perovskites.

In this contribution we report our determination of the limits of the composition x for which $La_{1+x}Sr_{2-x}Mn_2O_7$ is found by powder X-ray diffraction to exist as a single phase, crystallizing in the $I4/mmm$ space group. The evolution of the crystal structure with x has been followed by the Rietveld refinement of powder diffrac-

---

[⊗] Abstract published in *Advance ACS Abstracts,* October 1, 1996.

(1) Kusters, R. M.; Singleton, J.; Keen, D. A.; McGreevy, R.; Hayes, W. *Physica B* **1989**, *155*, 362.

(2) von Helmholt, R.; Wecker, J.; Holzapfel, B.; Schultz, L.; Samwer, K. *Phys. Rev. Lett.* **1993**, *71*, 2331.

(3) Mahendiran, R.; Mahesh, R.; Raychaudhuri, A. K.; Rao, C. N. R. *Solid State Commun.* **1995**, *96*, 515.

(4) Mahesh, R.; Mahendiran, R.; Raychaudhuri, A. K.; Rao, C. N. R. *J. Solid State Chem.* **1995**, *120*, 204.

(5) Maignan, A.; Simon, Ch.; Caignaert, V.; Raveau, B. *Solid State Commun.* **1995**, *96*, 623.

(6) Maignan, A.; Simon, Ch.; Caignaert, V.; Raveau, B. *C.R. Acad. Sci. Paris* **1995**, *t321, ser. IIb*, 297.

(7) Maignan, A.; Simon, Ch.; Caignaert, V.; Raveau, B. *Z. Phys. B* **1996**, *99*, 305.

(8) Hwang, H. W.; Cheong, S.-W.; Radaelli, P. G.; Marezio, M.; Batlogg, B. *Phys. Rev. Lett.* **1995**, *75*, 914.

(9) Mahendiran, R.; Tiwary, S. K.; Raychaudhuri, A. K.; Ramakrishnan, T. V.; Mahesh, R.; Rangavittal, N.; Rao, C. N. R. *Phys. Rev. B* **1996**, *53*, 3348.

(10) Tomioka, Y.; Asamitsu, A.; Moritomo, Y.; Kuwahara, H.; Tokura, Y. *Phys. Rev. Lett.* **1995**, *74*, 5108.

(11) Tomioka, Y.; Kuwahara, H.; Moritomo, Y.; Tomioka, Y.; Asamitsu, A. *Phys. Rev. Lett.* **1996**, *76*, 3184.

(12) Ramirez, A. P.; Schiff, P.; Cheong, S.-W.; Chen, C. H.; Bao, W.; Palstra, T. T. M.; Gammel, P. L.; Bishop, D. J.; Zegarski, B. *Phys. Rev. Lett.* **1996**, *76*, 3188.

(13) Shimakawa, Y.; Kubo, K.; Manako, T. *Nature* **1996**, *379*, 53.

(14) Cheong, S.-W.; Hwang, H. Y.; Batlogg, B.; Rupp Jr., L. W. *Solid State Commun.* **1996**, *98*, 163.

(15) Moritomo, Y.; Asamitsu, A.; Kuwahara, H.; Tokura, Y. *Nature* **1996**, *380*, 141.

(16) Mahesh, R.; Mahendiran, R.; Raychaudhuri, A. K.; Rao, C. N. R. *J. Solid State Chem.* **1996**, *122*, 448.

(17) Mohan Ram, R. A.; Ganguly, P.; Rao, C. N. R. *J. Solid State Chem.* **1987**, *70*, 82.

(18) Ruddlesden, S. N.; Popper, P. *Acta. Crystallogr.* **1958**, *11*, 54.

(19) Shaked, H.; Keene, P. M.; Rodriguez, J. C.; Owen, F. F.; Hitterman, R. L.; Jorgensen, J. D. *Crystal Structures of the High-T_C Superconducting Copper-Oxides*; Elsevier: Netherlands, 1994.

S0897-4756(96)00342-0 CCC: $14.00

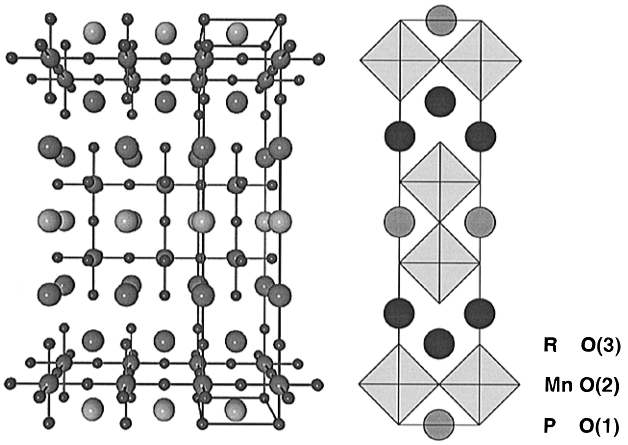

Figure 1. Crystal structure of $La_{1+x}Sr_{2-x}Mn_2O_7$, depicted for $x = 0.2$. The schematic polyhedral representation is also shown, with the atoms labeled.

tion data acquired for samples with diffeent values of x. This has been performed individually on each data set, as well as in a novel manner, in a single combined run. The motivation is as follows:

The XND Rietveld program[20] has been developed with the aim of analyzing multiple powder data sets. The idea is that when powder diffraction data collected at different temperatures, pressures, magnetic fields, etc. are analyzed by means of a functional (polynomial of arbitrary order) dependence between the refinable parameters at different temperatures (pressures, etc.) there results a considerable reduction of the number of parameters, allowing the use of poorer individual data sets for following the evolution of structural parameters. While the method is powerful, there exist very few actual applications in the literature.

Instead of using temperature as a variable in the refinement, we have used the composition variable x. For samples within the composition limits determined by us

$$La_{1+x}Sr_{2-x}Mn_2O_7 \qquad 0.1 \le x \le 0.45$$

we have analyzed nine X-ray powder data sets of relatively low resolution in one simultaneous refinement. This permits the description of a field of structures in one space group but for different compositions. To achieve this, we have had to make certain assumptions for the dependencies of the different parameters on x which we justify. Since studies of the evolution of structural parameters with composition are so important and ubiquitous in solid state chemistry, we feel that the technique presented here is of considerable general interest to the community.

We have referred to the presence of two sites in the structure that can be occupied by the A cations (La^{III} and Sr^{II}). The sites are either 12-coordinate (marked P in Figure 1) or 9-coordinate (marked R in Figure 1), occurring in the ratio 1:2. Unless the A cations are taken in this ratio and are sufficiently distinct from each other that they are able to order, they will inevitably distribute between the two sites. The X-ray scattering factors of La and Sr are quite different allowing the distribution to be reliably obtained even from powder X-ray data. In a previous publication,[21] we have shown that the distribution of cations within the two sites affect the structure and thus property. We follow this theme here and point out that the ability of the two cations to distribute between the two sites helps increase the adaptability of the structure. Earlier workers might have missed observing these effects in the “0212” structure because they refined the A atom occupancies in the two sites using pseudoatoms with suitable scattering factors (lengths) thereby smearing out the difference between the two A atoms.[22−25]

Within the composition range, we have studied the electrical resistivity and magnetization at 1.45 T as a function of temperature and present our understanding of the observed trends in terms of what we determine about the structure, as well as based on our knowledge of the related perovskites.

Experimental Section

The title phases were prepared by grinding La_2O_3, $SrCO_3$, and Mn_2O_3 taken according to stoichiometry. Bi_2O_3 was added as a sintering agent. The powders were fired in dense alumina crucibles initially at 1173 K for 12 h, following which they were reground and fired at 1473 K for 12 h. Finally, the powders were pressed into rectangular bars with the dimensions 2 × 2 × 10 mm and fired at 1773 K for 12 h. For the final firing, the temperature was ramped to and from 1773 K at a rate of 300 K/h. All the firings were carried out in air.

The addition of Bi improves sintering and ensures the formation of clean phases. To verify that the Bi had been volatilized after the final firing, SEM/EDS was carried out on a JEOL JSM840 microscope equipped with a Kevex energy-dispersive X-ray (EDS) analyzer. Phase formation was verified using a Guinier-deWolff X-ray camera. For the Rietveld analysis, X-ray data on powders was acquired in the Bragg−Brentano geometry on a Philips PW3710-based vertical diffractometer using Cu Kα radiation. The data were collected with a step scan 2θ interval of 0.02° or 0.04° in the range 4−100°. The counting time was fixed at 7 s per 2θ step. To minimize problems of background, eccentricity, and preferred orientation, the samples were sieved on to a groved aluminium sample plate through an ASTM 120-grade mesh, packed down and cut to the level of the sample plate using a sharp blade. Magnetization as a function of temperature was measured using a vibrating sample magnetometer. For the resistivity studies, copper leads were soldered onto bars of the samples using indium that was deposited ultrasonically.

Results and Discussion

Bi Addition. When the title phases are prepared without the addition of Bi but using the same thermal treatment, the bars obtained are not very well sintered and tend to crumble after a period of time. Both Guinier X-ray films as well as X-ray diffraction patterns indicate the presence of the perovskite, (La,Sr)MnO_3. Small amounts of Bi_2O_3 seem to serve as a flux and considerably assist both phase formation as well as densification. The bars obtained after Bi additions are well sintered

---

(20) Bérar, J.-F.; Garnier, P. *Accuracy in Powder Diffraction*; Proc. II Intl. Conf., Gaithersburg, 1992, and *NIST Special Publ.* **1992**, *846*, 212. The program and documentation are available by anonymous ftp from rx-crg1.polycnrs-gre.fr.

(21) Seshadri, R.; Martin, C.; Maignan, A.; Hervieu, M.; Raveau, B.; Rao, C. N. R. *J. Mater. Chem.* **1996**, *6*, 1585.

(22) Samaras, D.; Collomb, A.; Joubert, J. C. *J. Solid State Chem.* **1973**, *7*, 337.

(23) Attfield, M. P.; Battle, P. D.; Bollan, S. K.; Kim, S. H.; Powell, A. V.; Workman, M. *J. Solid State Chem.* **1992**, *96*, 344.

(24) Kim, I.-S.; Kawaji, H.; Itoh, M.; Nakamura, T. *Mater. Res. Bull.* **1992**, *27*, 1193.

(25) Ueno, S.; Meng, J.; Kamegashihara, N.; Saito-Nakano, H.; Enami, K. *Mater. Res. Bull.* **1996**, *31*, 497.

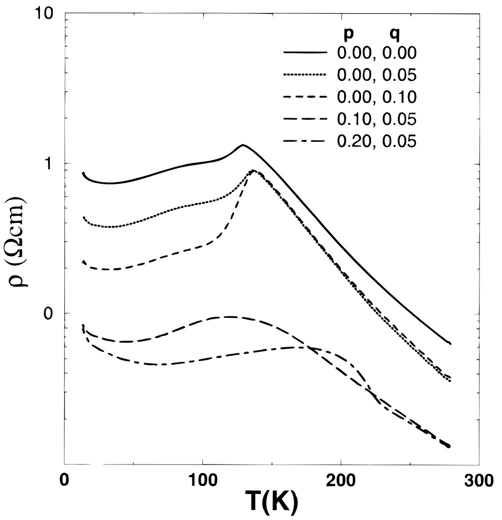

Figure 2. Resistivity as a function of temperature for bars of the phases with nominal cationic compositions corresponding to $La_{1.2-p}Bi_pSr_{1.8}Mn_2Bi_q$ with p and q marked in the figure.

and indefinitely stable in air. In the scanning electron microscope, they display a very compact, void-free morphology. Figure 2 displays the $\rho-T$ curves of bars of samples of initial cation composition $La_{1.2-p}Bi_p$-$Sr_{1.8}Mn_2Bi_1$, with p and q indicated in the figure. In these samples, we have tried to compare the effect of Bi as an additive and as a substituent. We see that the effect of small amounts of Bi ($p = 0$, $q = 0.05$, 0.10) as additive is to make the resistivity transition around 130 K sharper, indicating better sintering and possibly greater purity. When Bi is taken in the stoichiometry ($p = 0.10$, 0.20, $q = 0.05$), the change in the resistivity behavior is quite drastic, indicating that Bi could play an interesting role in transport, as already shown in the perovskite manganites.[26] From Figure 2 and the EDS analysis we can be confident that small amounts of Bi taken in excess do not enter the structure but are volatilized during the final firing. All samples were therefore prepared with a bismuth overstoichiometry according to the nominal formula $La_{1+x}Sr_{2-x}Mn_2Bi_{0.1}O_{7+\delta}$.

Phase Limits. The individual powder X-ray data sets for samples corresponding to $La_{1+x}Sr_{2-x}Mn_2O_7$ with $0.0 \lesssim x \leq 0.5$ were refined in the $I4/mmm$ space group. Plots of the lattice parameters as a function of x shown in Figure 3a,b as light lines and error bars suggested the presence of either a structural transition or phase separation in the regions $0 < x < 0.1$ and $0.45 < x < 0.50$. The patterns obtained for the phases with $x = 0.5$ showed reflections that could not be indexed in the $I4/mmm$ space group, and suggested the presence of the perovskites $(La,Sr)MnO_3$. While initially we felt that the phase with $x = 0$, namely, $LaSr_2Mn_2O_7$ is outside the $I4/mmm$ phase limit, we have recently become aware of work by Battle et al.[27] suggesting that the $x = 0$ phase retains this space group. We have since confirmed this by electron diffraction. The properties of this $x = 0$ phase are quite different however, meriting separate treatment.[28] It might be possible through different synthetic conditions to extend the phase limits.

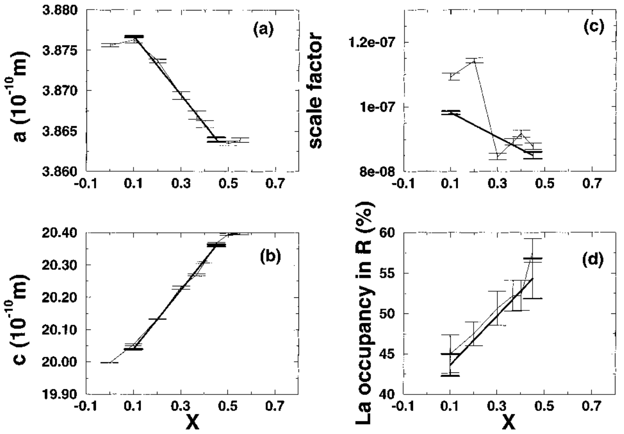

Figure 3. Parameters obtained from Rietveld refinement, plotted as a function of x for $La_{1+x}Sr_{2-x}Mn_2O_7$. The light lines and error bars correspond to the individual refinement and the heavy lines and error bars to the combined refinement. (a) The a parameter (in Å). (b) The c parameter (in Å). (c) The X-ray scale factor. (d) The percentage (in terms of total La) occupancy of La in the R site of the structure.

In this contribution we restrict ourselves to a description of the $I4/mmm$ phases $La_{1+x}Sr_{2-x}Mn_2O_7$ with $0.1 \leq x \leq 0.45$.

Structure Refinement. Since the strategy used to obtain and describe the structural evolution is novel, we have, as a first step, performed individual refinements of six powder X-ray data sets in the region of interest. In all the plots describing the evolution of structural parameters, the values obtained from these (individual) refinements are depicted using light lines and error bars. As mentioned earlier, the combined refinement is based on the strategy that the data obtained for samples with different x values can be refined using a model structure that evolves with x using polynomials in x to describe the parameters at the different x values. Instead of x as defined by the formulation $La_{1+x}Sr_{2-x}Mn_2O_7$, we have used $x' = x - 0.1$ so that the solubility limit is $0 \leq x' \leq 0.35$, and the origin, $x' = 0$ corresponds to the lower phase limit $La_{1.1}$-$Sr_{1.19}Mn_2O_7$. We have, for all the refinable parameters, except the thermal factors, started with the assumption that they vary linearly with x'. This is drastic but justified by the comparison of the combined refinement with the individual ones. The problem is thus one of determining the intercept at $x' = 0$ and the slope, for every refinable parameter in a refinement combining many data sets. We also attempted more complex evolutions, viz., quadratics in x' to describe the lattice parameters and scale factor. This usually resulted in poorer refinements due to greater correlation between the parameters. To describe the evolution of composition, it was necessary to describe the occupation of the P and R sites using eight atoms as shown in Table 1. The refinement codes have signs of + or − signifying accretion or depletion, respectively. This complex description is necessitated because we need describe both the change in composition (performed by the first block of four atoms), as well as the distribution of La and Sr between the P and R sites. The latter is performed by the second block of four atoms. The final position or

---

(26) Damay, F.; Maignan, A.; Hervieu, M.; Nguyen, N.; Raveau, B. *C.R. Acad. Sci. Paris* **1996**, *t322, ser. II*, 573.

(27) Battle, P. D.; Green, M. A.; Laskey, N. S.; Millburn, J. E.; Rosseinsky, M. J.; Sullivan, S. P.; Vente, J. F. *J. Chem. Soc., Chem. Commun.* **1996**, 767.

(28) Seshadri, R.; Maignan, A.; Hervieu, M.; Nguyen, N.; Raveau, B. *Solid State Commun.*, submitted.

Table 1. Description of P and R Sites in $La_{1+x}Sr_{2-x}Mn_2O_7$ in a Combined Rietveld Refinement of Powder X-ray Data[a] ($x' = x - 0.1$)

atom	z(const)	z(x′)	occupancy(const)	occupancy(x′)
LaP	0.5	0	0	1
SrP	0.5	0	0	−1
LaR	0.3175[15]	0.0007[52]	0	1
SrR	0.3175[15]	0.0007[52]	0	−1
LaP′	0.5	0	1.2362[13]	−0.7581[53]
SrP′	0.5	0	0.7638[−13]	0.7581[−53]
LaR′	0.3175[15]	0.0007[52]	0.9638[−13]	0.7581[−53]
SrR′	0.3175[15]	0.0007[52]	3.0362[13]	−0.7581[53]

[a] The numbers within square brackets are refinement codes; two values with the same code are refined together.

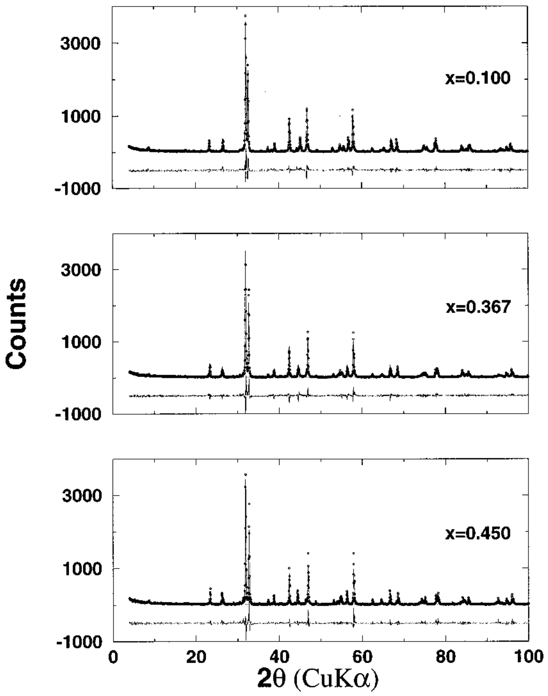

Figure 4. Typical X-ray diffraction data (points), refined profiles, backgrounds and difference profiles for $La_{1+x}Sr_{2-x}Mn_2O_7$, obtained from the combined refinement. The difference profiles have been offset by 500 counts for clarity. The values of x are shown in the figure.

occupancy for a given $x' = x - 0.1$ value is arrived at by adding the constant value (intercept) to the product of the coefficient of x' with x'.

The description of the profile parameters including peak widths, systematic zero shifts, preferred orientation, peak asymmetry, and background were lumped together in one block, assuming these were common for all nine data sets used. The backgrounds were verified to be much the same for all data sets and could be treated using linear interpolation between points far from Bragg peaks. The assumption of constant zero shift is rather drastic for the Bragg−Brentano geometry used and is possibly the source of poor reliability factors for certain data sets. Figure 4 shows the X-ray powder data (points), the refined profile, background, and difference profiles for three typical data. The refinement was performed in a combined manner. We see tht the errors in fitting the experimental data are largely errors arising from zero shifts and profile. Considering the simplicity of the model, the data seem to refine surprisingly well. An alternate possibility in the XND program allows for the datasets to be each treated with unique profile and background parameters. This considerably increases the number of parameters that need be refined without any significant gains, at least in this case.

Since the method is novel, it is necessary to compare the parameters obtained from the combined refinement with those obtained from traditional, individual refinements. In the four panels in Figure 3, we have compared the lattice parameter, scale factor and percentage La (in terms of total La) in the R site obtained from individual refinements (light lines, error bars) with the line (heavy) obtained from the combined refinement. Note that while the individual refinements yield points at different x values for the refinable parameters, the combined refinement yields a line, through the region studied.

From Figure 3, we see that the lattice parameters and occupancy refine very satisfactorily. While the $a-b$ plane is compressed on increasing x, the c parameter increases. The correspondence between the scale factors obtained in the two methods is not so good, reflecting, as pointed out earlier, the difficulty in reproducing experimental conditions in an X-ray powder data collection, particularly in the Bragg−Brentano geometry. The reason for the divergence of the error bars in the combined refinement at high x values is as follows. The combined refinement yields, for every refinable parameter, the values of the intercept c and the slope m, along with the 1σ errors δc and δm. The line and the error are thus for

$$y = mx' + c$$

calculated using

$$\delta y = \delta m x' + \delta c$$

The divergence in the error bar is an artifact of the x' dependence and can be reduced by shifting the origin of x' to the center of the region. We prefer not to do this because it reduces the clarity of the procedure for following evolution of the structure as presented here. As an origin, we could pick any point in the region of interest. There would be no reason for the values of $c(\delta c)$ or $m(\delta m)$ to change as a result of such a shift, but the value of δy would be minimum at the origin. In effect then, it is the minimum rather than the maximum error bar which represents the error. On this point, one of the referees has pointed out that a proper analysis of the error would take account of the correlation between m and c, and a more accurate estimate would be obtained by using

$$\delta c = \delta y/\sqrt{N} \qquad \delta m = \delta y/\sqrt{N-1}\Delta x'$$

where N is the number of datasets (here 9) and $\Delta x'$ the separation in x'. From this analysis, we obtain much smaller error bars on the parameters, close to the smallest uncertainties shown in the different figures. However, since the analysis of error is often a matter of choice, we retain the error bars displayed in the various figures as (rather pessimistic) limits on the uncertainty in the refined parameters.

From Figure 3d, we see that increase of x results in an increased occupancy of La in the R site. We discuss this effect further on.

In the structure of the title phases, there are four positional parameters that are refinable. In Figure 5a−

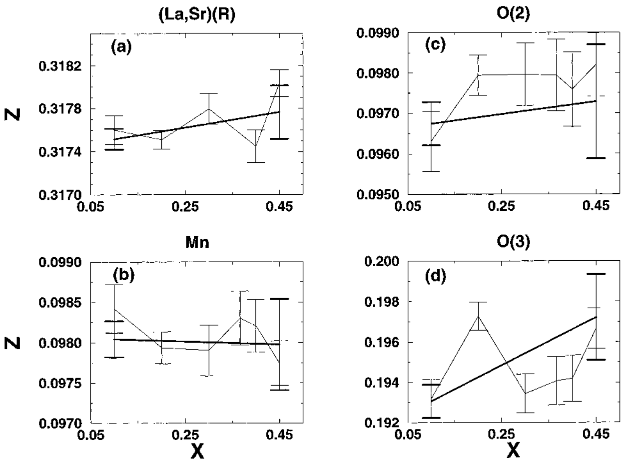

Figure 5. Positional parameters obtained from Rietveld refinement, plotted as a function of *x* for $La_{1+x}Sr_{2-x}Mn_2O_7$, following the convention in Figure 3. (a) The *z* position of (La,Sr) in the R site. (b) The *z* position of Mn. (c) The *z* position of O(2). (d) The *z* position of O(3).

Table 2. $La_{1+x}Sr_{2-x}Mn_2O_7$, $0.1 \le x \le 0.45$ Crystal Structures from a Combined Rietveld Refinement of Powder X-ray Data

space group: *I*4/*mmm* (No. 139)
$x' = x - 0.1$
$a = 3.8767(1) - 0.0363(5)x'$ Å, $c = 20.040(1) + 0.916(5)x'$ Å
$R_{\mathrm{Bragg}} = 9.7\%$, $R_{\mathrm{wp}} = 21.3\%$, $R_{\mathrm{F}} = 6.7\%$

atom	*x*	*v*	*z*	*B* (Å^2)[a]	occupancy[b]
La(P)	0	0	$^1/_2$	0.18(4)	$1.24(3) + 0.24(12)x'$
Sr(P)	0	0	$^1/_2$	0.18(4)	$0.76(3) - 0.24(12)x'$
La(R)	0	0	$0.3175(1) + 0.0007(4)x'$	−0.04(3)	$0.96(3) + 1.76(12)x'$
Sr(R)	0	0	$0.3175(1) + 0.0007(4)x'$	−0.04(3)	$3.04(3) - 1.76(12)x'$
Mn	0	0	$0.0981(2) - 0.0002(10)x'$	−0.22(3)	4
O1	0	0	0	0.5(3)	2
O2	0	$^1/_2$	$0.0967(5) + 0.002(2)x'$	0.2(1)	8
O3	0	0	$0.1932(8) + 0.011(4)x'$	1.8(2)	4

Details of Powder Data Used

x'	datapoints	2θ (deg)	R_{Bragg} (%)	GoF
0.000	2401	4.0−100.0	11.5	1.89
0.067	4651	7.0−100.0	5.3	1.55
0.133	2401	4.0−100.0	5.9	1.59
0.167	2401	4.0−100.0	12.2	1.57
0.200	2401	4.0−100.0	11.3	1.93
0.233	2401	4.0−100.0	8.2	1.72
0.267	2401	4.0−100.0	10.1	1.82
0.300	2401	4.0−100.0	11.8	1.88
0.350	2401	4.0−100.0	10.3	1.73

[a] *B* assumed not to change with x'. [b] Occupancy in cell; this is twice the occupancy in the formula.

d, we show the evolution of these with *x*, once again using light lines and error bars to describe the results of the individual refinements and heavy lines and error bars to describe the results of the combined refinements. The scatter arises because of the very small *y*-axis scale used and the relatively small changes in the values as *x* is varied.

Table 2 details the results of the combined refinement. Since the refinement itself depends on the composition variable $x' = x - 0.1$, Table 2 actually describes not one structure but a *structural field*. To our knowledge, this is the first time that the crystal structures of phases in one homogeneity (or solubility) range have been thus described. The overall values of the reliability factors are satisfactory. As mentioned earlier, the discrepancies are related to features of profile rather than structure. In the bottom of the table, we list the details of the data sets used along with the values of the reliability factors R_{Bragg} and goodness of fit obtained for each dataset from the combined refinement. The thermal parameters for Mn and the R site are negative and thus unsatisfactory. This reflects the limited dynamic range of the experiment rather than the method used, and the problem of poor thermal parameters prevails in the individual refinements. The 1σ uncertainties given in parentheses, when they refer to an x' dependence, should also be multiplied by the value of x'. Due to this we retain as significant, values of the x' dependence even when they are smaller than the uncertainty.

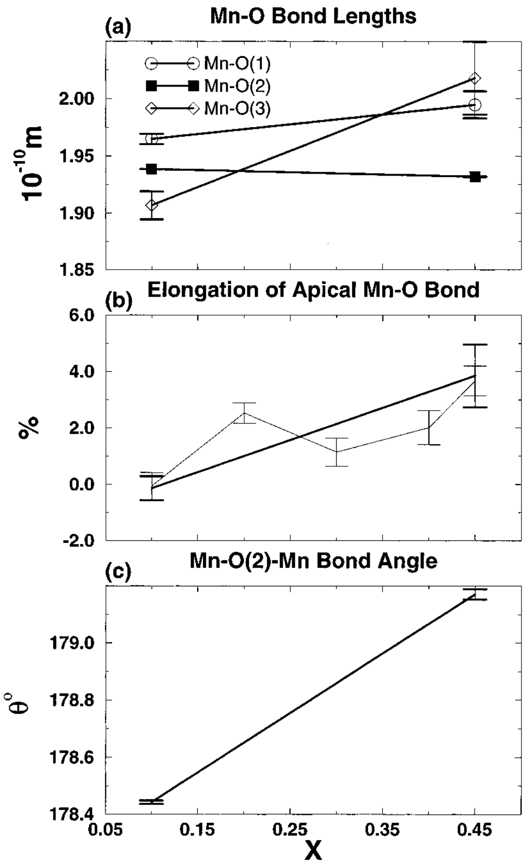

Figure 6. (a) Mn−O bond lengths (in Å) obtained from the combined refinement. The smaller error bars for Mn−O(2) reflects the greater precision in the determination of the *a* parameter. (b) Elongation of the apical Mn−O bond calculated according to

$$\frac{\frac{1}{2}\sum \overline{\mathrm{MnO}_{\mathrm{apical}}} - \overline{\mathrm{MnO}_{\mathrm{equitorial}}}}{\overline{\mathrm{MnO}_{\mathrm{equitorial}}}} \times 100$$

This is shown for individual as well as combined refinements. (c) Mn−O(2)−Mn bond angle as a function of *x*.

Features of the Structural Evolution. Figure 6 shows the evolution of the Mn−O bond lengths and angles with *x*. From Figure 6a, we see that while the equatorial Mn−O(2) bond length and the apical Mn−O(1) bond in the double-perovskite slab change very little, the length of the apical Mn−O(3) bond from Mn to the oxygen in the rock-salt layer of the structure changes significantly with *x*. The data in Figure 6a are results of the combined refinement. Increase of *x* in $La_{1+x}Sr_{2-x}Mn_2O_7$ implies increasing the amount of Mn^{III} which is an ion amenable to Jahn−Teller distortion. Figure 6b shows the percentage elongation of the apical Mn−O bond (the average of the Mn−O(1) and Mn−O(3) bonds) over the bond in the plane (Mn−O(2)). The data are from the individual as well as the combined refinement. Since the calculation of such elongation involves many refined parameters, Figure 6b is in essence the justification of the combined refinement. We observe a Jahn−Teller type elongation of the average apical Mn−O bond length as x is increased as expected from considerations of charge. The magnitude of the distortion is rather small in agreement with the results obtained for the 3D Mn perovskites $Pr_{0.7}Ca_{0.3-x}Sr_x$-MnO_3.[29,30] Figure 6c shows that the change in the Mn−O(2)−Mn bond angle across the stability range is almost negligible attesting to the adaptability of the structure across a wide range of Mn valence. This is in strong contrast to many Mn perovskites;[8,31] more specifically to the perovskites $La_{1-x}Sr_xMnO_3$.[32]

The most remarkable features of the evolution of the structure with $x' = x - 0.1$ is the retention of a nearly 180° Mn−O(2)−Mn bond angle and the approximately constant size of the double perovskite unit in terms of an approximately constant Mn−O(1) bond length. In an earlier publication[21] on the system $RE_{1.2}Sr_{1.8}Mn_2O_7$, with RE = La,Pr,Nd, we had remarked the correlation between the increase in the Mn−O(3) bond length as the size of RE is decreased and the greater occupancy of the smaller rare-earth ions in the 9-coordinate rock-salt (R) site of the structure. This correlation is also seen across the series $La_{1+x}Sr_{2-x}Mn_2O_7$ presented here. La^{III} is smaller than Sr^{II} and we observe from Figures 6a and 3d that an elongation of Mn−O(3) correlates with increased La occupancy in the R site. However, the observation of a nearly constant Mn−O(2)−Mn bond angle and Mn−O(1) bond length suggests that such correlation might be an effect rather than a cause. The structure is clearly trying to retain the integrity of the double perovskite unit. We have tried to understand this by considering the average volumes of the ions occupying the P site. This is akin to considerations of the Goldschmidt tolerance in perovskites. In Figure 7, we have plotted the percentage change in the average volumes (calculated from 12-coordinate Shannon[33] radii) as a function of x. The solid line represents the volume obtained from the refined evolution, while the dashed line assumes that the occupancy of La and Sr in the P site are initially as refined for $x = 0.1$ but the new La entering the structure distributes equally between the P and R sites. There seems to be a significant tendency in the structure to keep the volume of the P site constant, and this is achieved by a "pumping" of volume; pushing more Sr^{II} into this site. The importance of this effect is that transport properties of the manganites depend crucially on the Mn−O−Mn bond angles. Particularly in these quasi-2D systems, the flatness of the perovskite block would imply much freer conduction as is observed in layered cuprates where T_C shows a direct correlation to the absence of distortion of the CuO_2 sheets.[34]

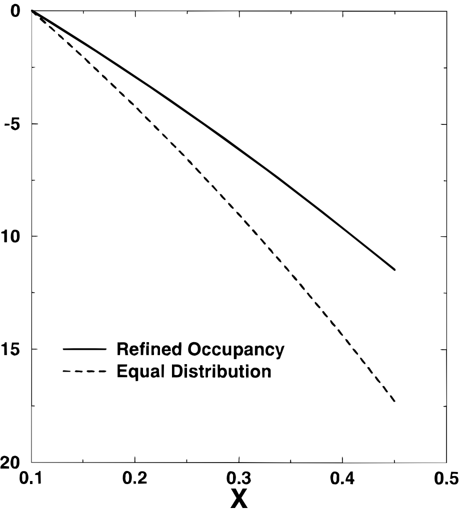

Figure 7. Calculated percentage change in volumes of ions in the P site as a function of x.

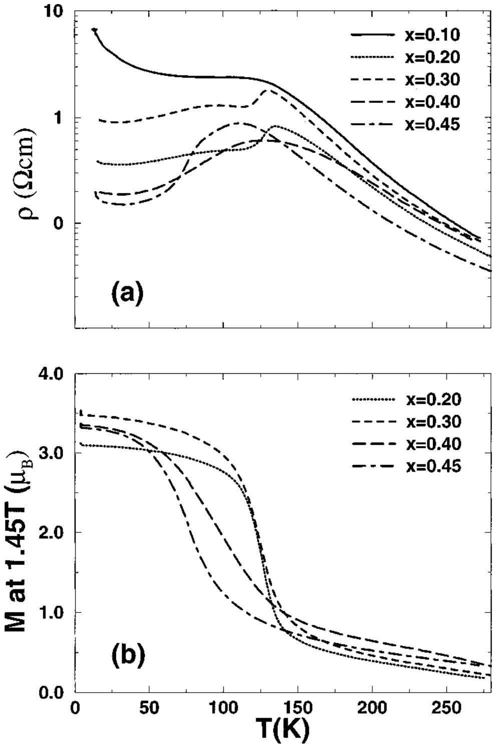

Figure 8. (a) Resistivity as a function of temperture for phases in the system $La_{1+x}Sr_{2-x}Mn_2O_7$. (b) Magnetization per Mn under a 1.45 T field as a function of temperature.

Electrical and Magnetic Properties. Figure 8a shows representative $\rho-T$ curves, and Figure 8b, the magnetization per Mn under a 1.45 T field as a function of temperature of the title phases. As in other perovskite manganites, the insulator−metal transition, characterized by the temperature coefficient of resistance changing sign from negative to positive, is accompanied by a transition to a state with predominantly ferromagnetic correlations (seen in Figure 8b). This is due to charge carriers hopping with spin conservation. Sharp transitions in the $\rho-T$ curves seen for $x = 0.2$ and $x = 0.3$ are complemented by sharp transitions to a ferro-

---

(29) Caignaert, V.; Suard, E.; Maignan, A.; Simon, Ch.; Raveau, B. *C.R. Acad. Sci. Paris* **1995**, *t321, ser. IIb*, 515.

(30) Caignaert, V.; Suard, E.; Maignan, A.; Simon, Ch.; Raveau, B. *J. Magn. Magn. Mater.* **1996**, *153*, L260.

(31) Radaelli, P. G.; Marezio, M.; Hwang, H. Y.; Cheong, S.-W. *J. Solid State Chem.* **1996**, *122*, 444.

(32) Urushibara, A.; Moritomo, Y.; Arima, T.; Asamitsu, A.; Kido, G.; Tokura, Y. *Phys. Rev. B* **1995**, *51*, 14103.

(33) Shannon, R. D. *Acta. Crystallogr. A* **1976**, *32*, 751.

(34) Dabrowski, B.; Wang, Z.; Rogacki, K.; Jorgensen, J. D.; Hitterman, R. L.; Wagner, J. L.; Hunter, B. A.; Radaelli, P. G.; Hinks, D. G. *Phys. Rev. Lett.* **1996**, *76*, 1348.

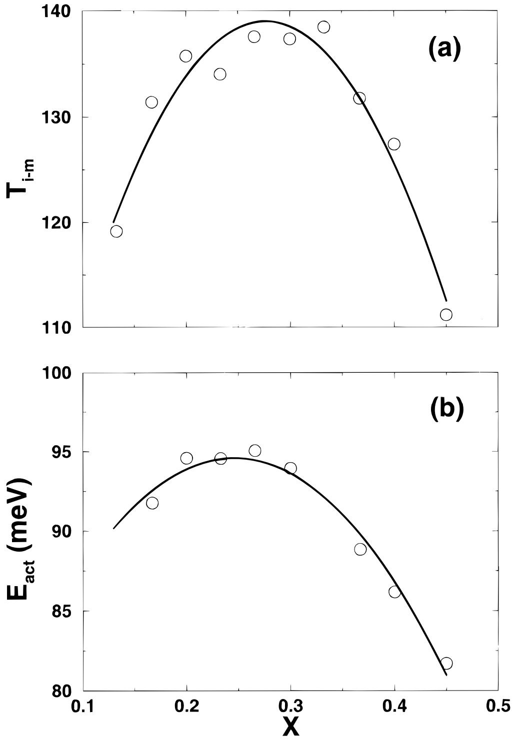

Figure 9. (a) Temperature of the insulator−metal transition as evidenced from a change in the sign of the temperature coefficient of resistance, plotted against x for the different phases in $La_{1+x}Sr_{2-x}Mn_2O_7$. (b) Activation energy of electrical transport obtained from the $\rho-T$ curves at high temperatures, plotted against x.

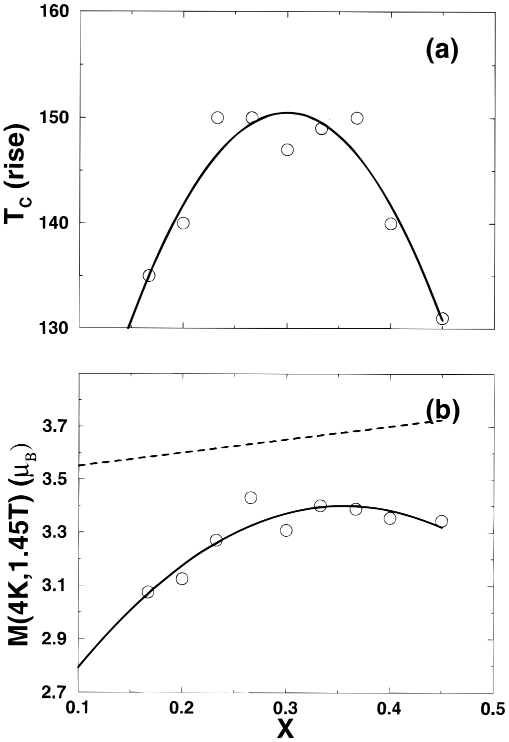

Figure 10. (a) Temperature at which the magnetization curves rise sharply, for the different $La_{1+x}Sr_{2-x}Mn_2O_7$ phases. Note the correspondence with Figure 9a. (b) Magnetization at 4 K per Mn under a 1.45 T for the different phases. The broken line corresponds to the spin-only value.

magnetic state. Just below the first transition at around 130 K in the resistivity, we observe another hump for some of the x values. This feature is not seen in single crystals[15] and could arise from the averaging of orientations, or due to grain boundaries in these polycrystalline samples. Near the limits at $x = 0.1$ and $x = 0.45$ the transitions are broader in both the magnetization as well as the resistivity, and the second hump in the resistivity is masked. An interesting feature of all the samples is the rise in resistivity at low temperatures (below 20 K), indicating a transition to a new insulating state.

The important feature of the resistivity and magnetization studies are that through the entire $I4/mmm$ composition range investigated, the systems show ferromagnetic correlations and a complementary insulator−metal transition. Figure 9a shows the temperature of the insulator−metal transition T_{i-m} obtained from the peak in the $\rho-T$ curves of the different samples, plotted as a function of x. The curve is a quadratic guide to the eye. The $T_{i-m}-x$ curve resembles the behavior found by Goodenough[35] in many perovskite manganites. In the perovskites, understanding curves such as the one shown in Figure 9a involve following changes in bond angles and sometimes space groups as well as the number of charge carriers. The adaptability of the title phases ensuing from the ability to "pump" cation volume from one site to another, results in relatively minor changes in the bond angles and almost negligible distortion of the MnO_6 octahedra across the composition range. The evolution of T_{i-m} with x in Figure 9a is thus largely dictated by the electron count. It is interesting that the energy of activation for electrical transport, obtained from the insulating, high-temperature part of the $\rho-T$ curves parallels the behavior of T_{i-m}. If E_{act} is indicative of the size of the bandgap, this is contrary to what one expects, since the more metallic systems (with smaller E_{act}) are expected to display higher T_{i-m}.

Figure 10a shows the temperature at which the magnetization under a 1.45 T field starts to rise sharply, plotted against x. The purpose of Figure 10a is to confirm the complementary behavior of the resistivity and magnetization by comparison with Figure 9a. In Figure 10b, we have plotted the saturation magnetization at 4 K under a field of 1.45 T as a function of x. The broken line is the expected spin-only value for an ideal ferromagnet. Again, the behavior is seen to resemble the empirical phase diagram of Goodenough[36] for the perovskite manganites $La_{1-x}Ca_xMnO_3$, except that in no portion of the phase diagram does the saturation magnetization reach the spin-only value. This could be the effect of reduced dimensionality. We note that as in the perovskites, the samples with saturation moments closer to the spin-only value show sharper transitions in both the $\rho-T$ curves as well as in the temperature dependence of magnetization.

Conclusions

Refinement Methodology and Contraindications. We present a new way of obtaining structural evolution with composition from powder data which is not necessarily of high quality and likewise a new way

---

(35) Goodenough, J. B. In Reiss, H., Ed. *Progress In Solid State Chemistry*; Pergamon: New York, 1971; Vol. 5.

(36) Goodenough, J. B. *Magnetism and the Chemical Bond*; Wiley-Interscience: New York, 1963.

of presenting the data. The assumption of a polynomial dependence has the effect of masking out subtle but abrupt changes in structure across the evolution and should not be used without first ensuring that abrupt changes are not taking place. Obviously, the method would fail completely if used across a phase transition. In XND though, the transformation of one phase to another can be handled, treating the scale factor like an order parameter. The advantages that ensue from the combined refinement are evident, including improved stability and a compact description of the structure. These advantages must be weighed against the possibility of errors being propagated by the combining of datasets. The use of other geometries for collecting X-ray data, particularly Debye−Scherrer, where eccentricity, zero shifts, and background usually vary less between experiments, is likely to yield better refinements. The technique is extremely amenable to the treatment of neutron data for the same reason.

Structure Property Correlations. The title phases are characterized by their being able to adapt to a wide range of manganese valence in contrast to the perovskites, where changes of size or charge result in changes of structure, and particularly, large distortions in the MnO_6 octahedra. This makes the interpretation of the electrical transport and magnetic properties somewhat easier in the title phases, the changes being dictated largely by electronic configuration. The magnetic phase diagram is characterized by a dome-shaped region below which the system shows predominantly ferromagnetic correlations. In this region, until a lower limit of about 20 K, the system displays metallic behavior as evidenced by the temperature coefficient of resistance. Below 20 K the systems become insulating once again, seen as an upturn in the resistivity. Throughout the region studied the sharpest transitions to the ferromagnetic state in the magnetization and to a metallic state in the resistivity, are shown by the phases with a nominal Mn valence between 3.2 and 3.4. In this smaller regime, the saturation magnetization is also closer to the ideal, spin-only value.

In light of the considerable interest generated by the observation of giant negative magnetoresistance in the perovskite manganites, we suggest that the layered maganites presented here provide relatively simple proving grounds for theories for the magnetoresistance and other magnetostructural phenomena. The adaptability of the structure points to a factor that needs to be considered in the rational design of new solids, namely, preferential distributions of cations according to size, between sites that are normally considered to be random alloys. Anomalous X-ray diffraction studies on powders at a synchrotron source are planned in order to assess the reliability of the refinement of cation occupancies as presented here. For consistency of argument, we have ensured that the discussion of the structural evolution in the title phases does not rely the refinement technique used.

Acknowledgment. This work was supported by the European Community Contract CI1*-CT94-0107. R.S. is grateful to Dr. J.-F. Bérar and Dr. G. Baldinozzi for their invaluable help. We are grateful to Dr. J. P. Attfield, one of the referees of this paper, for his insightful comments, particularly on the analysis of error.

CM960342X